metals

MDPI

Article

Fabrication, Microstructure, Mechanical, and Electrochemical Properties of NiMnFeCu High Entropy Alloy from Elemental Powders

Ashok Kumar [1], Michael Mucalo [2], Leandro Bolzoni [1], Yiming Li [3], Fantao Kong [4,*] and Fei Yang [1,*]

[1] Waikato Centre for Advanced Materials and Manufacturing, School of Engineering, University of Waikato, Hamilton 3240, New Zealand; ak307@students.waikato.ac.nz (A.K.); leandro.bolzoni@waikato.ac.nz (L.B.)
[2] School of Science, University of Waikato, Hamilton 3240, New Zealand; michael.mucalo@waikato.ac.nz
[3] Key Laboratory of Advanced Metals and Materials of Inner Mongolia, School of Materials and Metallurgy, Inner Mongolia University of Science and Technology, Baotou 014010, China; liyiming@imust.edu.cn
[4] School of Materials Science and Engineering, Harbin Institute of Technology, Harbin 150001, China
* Corresponding author: kft@hit.edu.cn (F.K.); fei.yang@waikato.ac.nz (F.Y.)

Abstract: Transition metal based high entropy alloys (HEAs) are often used in electrocatalytic (water electrolysis) applications due to the synergistic effect operating among its constituent elements and unpaired electrons in d orbitals of the concerned metal. In this study, a low cost NiMnFeCu high entropy alloy was successfully synthesised using the combined techniques of mechanical milling (MA) and vacuum sintering. X-ray diffraction was used to analyse the phase composition, optical microscopy, and scanning electron microscopy were used to characterise the fabricated material's microstructure and chemical homogeneity, thermal, and mechanical properties were tested using the differential scanning calorimetry method and a universal testing machine, respectively. Electrochemical workstation was used to carry out preliminary electrochemical studies such as linear sweep voltammetry (LSV), cyclic voltammetry (CV) and chronoamperometry. The results showed that the as- sintered NiMnFeCu HEA possessed a single- phase FCC structure. The HEA NiMnFeCu sintered at 1050 °C (S4) and 1000 °C (S2) with a holding time of 2 h showed a yield strength of 516.3 MPa and 389.8 MPa, respectively, and the micro-hardness values were measured to be 233.45 ± 9 HV and 198.7 ± 8 HV, respectively. Preliminary electrochemical studies proved that the alloy sintered at 1000 °C (S2) with a holding time of 2 h exhibited excellent electrocatalytic properties with a measured overpotential of 322 mV at 10 mA cm^{-2} at 100 cycles of CV and good stability for 10 h when compared to state-of-the-art electrocatalytic materials IrO_2 and RuO_2. This suggested that the HEA NiMnFeCu fabricated under the condition S2 could potentially be used for industrial-scale water electrolysis as it possesses permissible mechanical and good electrochemical properties.

Keywords: high entropy alloys; powder metallurgy; vacuum sintering; microstructure; oxygen evolution reaction

Citation: Kumar, A.; Mucalo, M.; Bolzoni, L.; Li, Y.M.; Kong, F.T.; Yang, F. Fabrication, Microstructure, Mechanical and Electrochemical Properties of NiMnFeCu High Entropy Alloy from Elemental Powders. *Metals* **2022**, *12*, 167. https://doi.org/10.3390/met12010167

Academic Editor: Soran Birosca

Received: 11 December 2021
Accepted: 13 January 2022
Published: 17 January 2022

1. Introduction

High entropy alloys (HEAs) are a new paradigm in designing alloys that have gained significant research interest in the last decade. HEAs consist of at least four or five principal elements with each element having a concentration of 5–35% in atomic% units [1]. Contrary to conventional alloys, HEAs possess high mixing entropy and form a simple random solid solution with cubic crystal structures (FCC and BCC) [2,3]. HEAs have very attractive properties that cannot be seen in conventional alloys, such as high strength and hardness [4–10], excellent wear-resistance [11–13], good fatigue and toughness [14–16], as well as good corrosion and oxidation resistance [17]. They also show

good mechanical properties from room temperature to even cryogenic temperatures [18]. These unique properties are attributed to the four core effects present in HEAs, namely the high entropy effect, the sluggish diffusion effect, the lattice distortion effect, and the cocktail effect [2].

Rapid depletion of fossil fuels and related environmental concerns have created a need for the development of an eco-friendly alternative energy source. Hydrogen is considered to be an effective clean energy carrier. Water electrolysis (water splitting) is an effective technique for producing hydrogen because it has effectively zero emissions [19]. However, this technique is confronted with several challenges. The existing state-of-the-art in electrocatalytic materials, namely RuO_2 and IrO_2, are very expensive materials to produce because of their lower natural abundance. Hence, extensive research is being carried out to replace these rare earth materials with cheaper alternatives [20,21]. Recently, transition element (group VIII 3d) based HEAs are being studied for water splitting applications due to the existence of the cocktail effect among its constituent elements. In addition, the presence of unpaired electrons in the d orbital can easily bond the ligands (OH^-) onto the surface of the catalyst [22]. The presence of multi-principal metallic components in HEAs can be used to customise the number of unpaired d electrons in the given catalyst. Compositional randomness promotes charge transfer (via surface adsorption/desorption processes) more effectively, thereby increasing the catalytic activity. HEAs possess many possible atomic arrangements, hence it offers more surface-active sites [23]. For instance, it has been shown by other researchers that the HEA MnFeCoNi exhibited a low overpotential value of 302 mV to reach a current density of 10 mA cm^{-2} with good stability for 20 h [24]. A porous HEA CoCrFeNiMo with a magnesium space holder exhibited excellent catalytic activity with an overpotential of 220 mV and attained a current density of 10 mA cm^{-2} with good stability for 24 h [25]. Hence HEAs could be considered as a cheaper alternative to a rare earth-metal catalyst. Several processing techniques have been reported for synthesising HEAs that are intended for water splitting reactions. Among these, mechanical alloying (MA) [24,26], casting [27,28], fast moving bed pyrolysis [29], electrochemical synthesis [30], and de-alloying [23,31] are very common methods used. Most reported HEAs for water splitting reaction contain expensive raw materials like cobalt [24,28]. In this work, we report a cobalt free, cheap NiMnFeCu HEA fabricated by combined mechanical alloying and vacuum sintering techniques, which is intended for electrocatalytic (water splitting) applications. The selected HEA could be employed as an alternative material for other electrocatalytic HEAs, which contain expensive raw materials like cobalt [27,28,31].

2. Experimental Methods

2.1. Materials Preparation

The starting materials used were elemental Ni (<50 μm, spherical), Mn (45 μm, irregular), Fe (<10 μm, spherical), and Cu (<75 μm, dendritic) powders, and all the powders had a purity >99% and were supplied by (Sigma Aldrich, St. Louis, MO, USA) company. The powders were firstly measured in desired weight proportions to make a high entropy alloy (HEA) NiFeMnCu and then placed into a milling vial with stainless steel balls, with a ball-to-powder ratio of 10:1, and a process control agent (PCA, with a ratio of 3 mL ethanol (PCA) per 75 g of powder) in a box under a protective argon environment. The mechanical milling was carried out using high-energy ball milling equipment (Fritsch Pulverisette -6, Idar-Oberstien, Germany), at a speed of 350 rpm for 5–20 h. The as-milled powders were taken out from the milling vial every 5 h for analysis. The 20 h as-milled powder was then cold-pressed into a green compact (the relative green density was about 67%) using a graphite lubricated cylindrical-shaped steel die with a diameter of 20 mm under an uniaxial pressure of 700 MPa at room temperature. Subsequently, the green compacts were placed in a vacuum furnace and sintered at the

desired temperature (1000 °C and 1050 °C) for a period of 1–2 h under a vacuum of about 10^{-3} Pa. The heating rate was maintained at 10 °C/min.

2.2. Material Characterization

The density of the as-sintered samples was measured using a gas pycnometer. A (Panalytical Empyrean X'pert X-ray powder diffractometer, Malvern, United Kingdom) with Cu Kα (λ = 0.154157 nm) radiation being used to identify the crystal structure of the as-milled powders and the as-sintered samples. A particle size analyser Malvern Mastersizer 3000 (also from Malvern, United Kingdom) was used to determine the particle size distribution of the as-milled powder. Microstructural observation for both the as-milled powders and the as-sintered samples was carried out by using optical microscopy (OM, Olympus BX 60, Tokyo, Japan) and scanning electron microscopy (SEM, Hitachi S4700, Tokyo, Japan) equipped with energy dispersive spectroscopy. The OM and SEM samples were prepared following these steps: (1) the as-milled powders were cold mounted using an epoxy resin, (2) the mounted samples were ground using SiC papers from 300 grit to 4000 grit, and (3) OP-S Non dry (colloidal silica) was used for final polishing of the ground samples. ImageJ was used to do the microstructural analysis for porosity.

2.3. Thermal Properties

Differential scanning calorimetry (DSC) was used to analyse the 20 h as-milled NiMnFeCu powders using the thermo-gravimetric analysis instrument (Netzsch Jupiter STA 449 F5, Frankfurt, Germany), to identify the possible phase transformation temperature. The heating rate was 10 °C / min, and the tested temperature range was from room temperature (25 °C) to 1400 °C.

2.4. Mechanical Testing

Vickers micro-hardness measurements were conducted using a micro-hardness tester (LM-700, Leco Ltd, St. Jospeh, MI, USA) under a load of 1 kg force (9.80 N) for 15 s. Measurements were performed at 10 different positions of the sample and the mean and standard deviation of the values were taken as the final hardness. Cylindrical specimens (4 mm diameter, 6 mm height) were employed for compression testing at room temperature using a universal testing machine (Instron 5982, Norwood, MA, USA) with a strain rate of 10^{-3} s^{-1}. Two samples were tested, and their mean and standard deviation of compressive yield stress values were recorded.

2.5. Electrochemical Testing

Electrochemical measurements were carried out using an eDAQ e-corder 410 electrochemical potentiostat, (New South Wales, Australia) with a standard three-electrode system. As-sintered NiMnFeCu (dimensions, 10 mm × 10 mm) was used as a working electrode, a Pt wire as the counter electrode, and a standard Ag/AgCl (Radiometer red rod) as the reference electrode in 1 M KOH solutions. The potential data were converted to reversible hydrogen electrode (RHE) referenced values according to the equation E (RHE) = E (Ag/AgCl) + 0.0591pH + 0.197 V), and the pH value of 1 M KOH solution was measured using an electronic pH meter with the pH being found to be approximately 13.8. Linear sweep voltammetry (LSV) was performed to measure the overpotential of the oxygen evolution reaction (OER) on samples with a scan rate of 5 mV s^{-1}. The overpotential (η) was measured using the formula η = E (RHE) − 1.23 V. The Tafel slopes were derived from the linear region of the LSV curves and fitted using the Tafel equation $\eta = b \log j + a$ (where b is the Tafel slope and j is the current density and a is an intercept related to current density). Cyclic voltammetry (CV) was carried out in the potential range (1.1–1.3) V vs. RHE for 100 cycles. The stability of the working electrode

was measured using a chronoamperometry technique at a potential of 1.7 V vs. (RHE) for 10 h.

3. Results and Discussion

3.1. Prediction of Phase Formation for the Designed HEA NiMnFeCu

There are several factors that contribute to the phase formation in HEAs [32]. Among them, the atomic size difference δ, mixing enthalpy ΔH_{mix}, configurational entropy ΔS_{config}, and valence electron configuration (VEC) all have a profound effect on the solid solution formations.

The thermodynamic parameters for solid solution formation in HEA NiMnFeCu were calculated using Equations (1)–(6).

$$\delta = 100\% \sqrt{\sum_i^n C_i} \left(1 - \frac{r_i}{\bar{r}}\right)^2, \quad (1)$$

where $\bar{r} = \sum_i^n C_i r_i$ and numerical factor 100 is used to amplify the data for more clarity and C_i is the molar fraction and r_i is the atomic radius of the i^{th} element in HEA

$$\Delta H_{mix} = 4 \sum_{i=1, i \neq j}^{n} H_{AB} C_i C_j, \quad (2)$$

where H_{AB} is the enthalpy of mixing of the binary alloy [33] and C_i C_j are the molar fractions of i^{th}, j^{th} element of the binary alloy

$$\Delta S_{config} = -R \sum_{i=1}^{n} C_i Ln C_i, \quad (3)$$

where R is the universal gas constant, 8.314 J $K^{-1}mol^{-1}$.

Solid solutions are likely to form when $-15 < \Delta H_{mix} < 5$ kJ/mol and $1 < \delta < 6.6\%$ [34]. An additional parameter Ω, which combines ΔH_{mix} and ΔS_{mix} and compares their relative weights by means of a ratio can be represented as

$$\Omega = \frac{T_m \Delta S_{config}}{\Delta H_{mix}}, \quad (4)$$

$$T_m = \sum_i^n C_i T m_i, \quad (5)$$

where T_m is the average melting temperature of the constituent elements of the HEAs. HEAs are formed when $\Omega \geq 1.1$ and $\delta \leq 6.6\%$ [34].

Valence electron concentration (VEC) is calculated using Equation (6)

$$VEC = \sum_i^n C_i \ VEC_i, \quad (6)$$

where VEC_i is the valence electron configuration of the i^{th} component in HEAs. HEAs would likely form an FCC crystal structure when VEC > 8 and a BCC structure when VEC < 6.87. If VEC is between 6.87 and 8, both FCC and BCC coexist in the fabricated HEAs [35].

The d electron count, which is used to predict the catalytic activity, was calculated using Equation (7) [36].

$$d\ electron\ count = Group\ number - Oxidation\ state. \quad (7)$$

Table 1 summarises the calculated thermodynamic–geometric parameters for phase formation in HEAs and the predicted d electron count of the designed NiMnFeCu HEA. It could be seen that the designed NiMnFeCu will form a random solid solution with an FCC crystal structure.

Table 1. Calculated thermodynamic- geometric parameters of HEA NiMnFeCu.

HEA	ΔS_{config} $J\ K^{-1}\ mol^{-1}$	ΔH_{mix} kJ/mol	δ	VEC	d-electron	Ω
NiFeMnCu	11.526	2.75	3.4	9	6.5	6.7

3.2. Phase Evolution during Mechanical Milling

Figure 1 depicts the XRD patterns of the as-milled NiFeMnCu alloy powders at a time interval of 5 h during the mechanical milling. After 5 h of mechanical milling, the peaks of the individual starting elemental powder disappeared completely and only the principal diffraction peaks at 2θ values 42.8°, 49.7°, 73.19°, 88.6°, and 94.2° could be seen. These peaks were indexed as (111), (200), (220), (311), and (222) and correspond to a single phase FCC structure. When continuing milling the powders for times extending to 10, 15, and 20 h, the principal diffraction peaks of FCC crystal structure remained unchanged. This implied that the NiMnFeCu HEA forms after 5 h of milling. This phenomenon is attributed to the dissolution of the starting elements and formation of the solid solution [37]. Continuous milling to extended times of 10, 15, and 20 h caused no further change in the diffractions peaks, which suggests that there was no further phase change. It is reasoned that the formation of the FCC phase in the studied NiMnFeCu HEA could be due to the presence of excessive FCC forming elements, as it is reported elsewhere that the alloying elements could be grouped into two categories, one being the FCC forming elements such as Cu, Ni, Co, and Mn, and the other being the BCC forming elements, such as Al, Cr, W, Fe, and V [38]. In addition to the calculated VEC of NiMnFeCu being 9, as discussed in the Section 3.1., this factor also resulted in the formation of the FCC structure in the studied HEA.

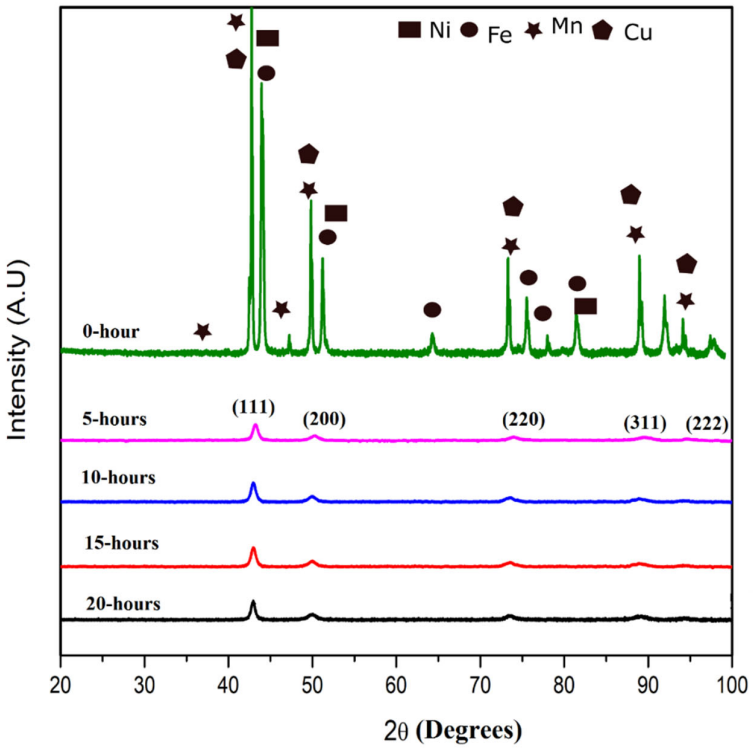

Figure 1. XRD patterns of the as-milled NiMnFeCu powders at various time intervals.

3.3. Effect of Milling Time on Powder Particles

Figure 2a–d shows the SEM images of the raw elemental powders and Figure 2e–h shows the SEM images of the as-milled powders at various times. It was observed that the raw elemental powders have varied morphology (Mn—irregular shape, Cu—dendritic shape, Ni and Fe—spherical shape). After milling for 5 h, the morphology of the as-milled powders showed irregular shapes and the powder particle size was observed to be about 105 microns (D50). After prolonging the milling time to 10, 15, and 20 h, the morphology of the as-milled HEA NiMnFeCu remained unchanged, however the particle size changed dramatically. With an increase in the milling time, the particle size of the as-milled powders decreased continually, with a value of 99.3 microns (D50) observed for the 10 h as-milled powders, 73.2 microns (D50) for the 15 h as-milled powders, and 42 microns (D50) for the 20 h as-milled powders, respectively. The variation of the powder particle sizes for the as-milled powders with milling time is presented in Figure 3 (the average particle size of the starting powders is about 20 microns (D50).

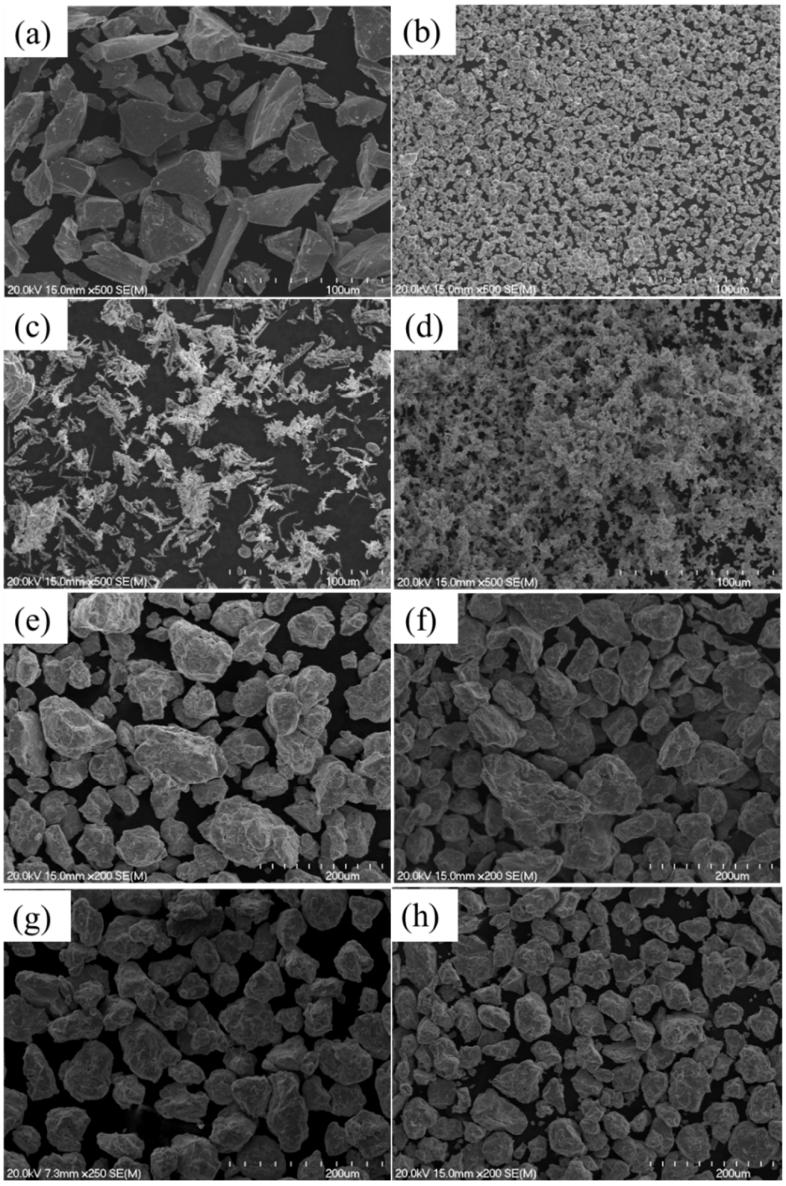

Figure 2. SEM micrographs of raw elemental powders and as-milled HEA NiMnFeCu at various time intervals. (**a**) Mn, (**b**) Fe, (**c**) Ni, (**d**) Cu, (**e**) 5 h, (**f**) 10 h, (**g**) 15 h, (**h**) 20 h.

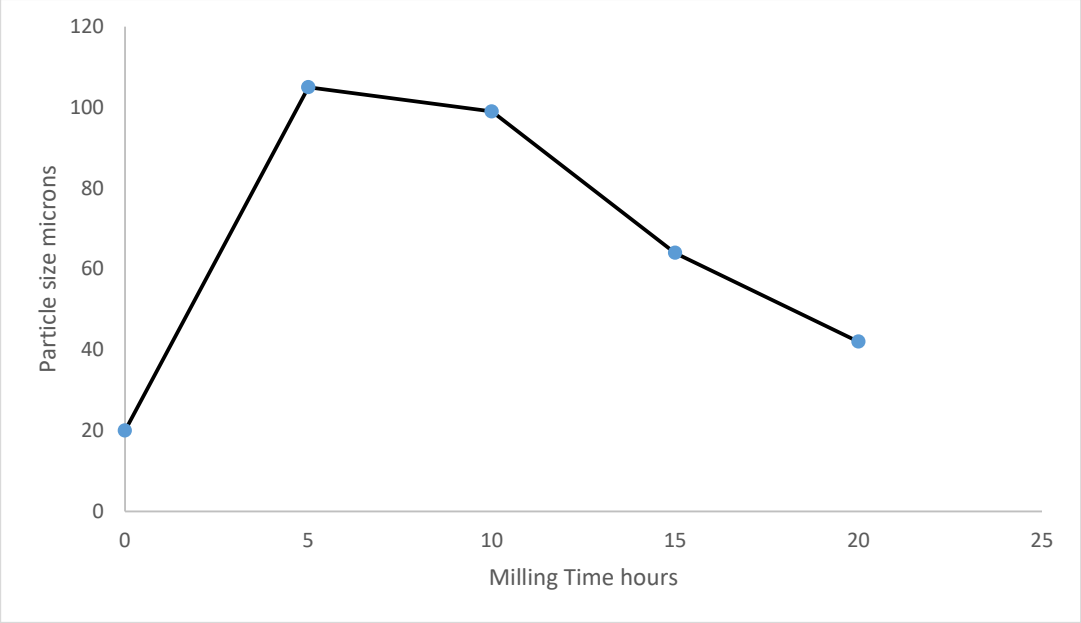

Figure 3. Particle size of the as-milled NiMnFeCu powders as a function of milling time.

Table 2 summarises the effect of milling time on the powder yield of NiMnFeCu. It can be seen that the powder yield after 5 h milling is very low, only reaching 44%. By increasing the milling time, the powder yield is continually increased. The powder yield is over 90% after 15 h of milling, and with the powder yield reaching 97% after a 20 h milling time.

Table 2. Effect of milling time on powder yield of NiMnFeCu powders.

Milling Time (h)	Weight of the Vial (g)	Weight of the Balls (g)	Powder Yield %
0	3123	700	-
5	3143	720	44
10	3133	715	64
15	3125	702	90
20	3124	701	97

The significant increase of the as-milled powder particle size from 20 microns (average particle size of starting powder) to 105 microns (for 5 h as-milled powders) suggest that the milling is at initial stages within the 5 h. This suggests that the cold-welding effect is dominant in this stage, which causes the particle size to coarsen. The low powder yield also confirms that the powders were severely stuck on the balls and the vial because of this cold-welding effect. With an increase in the milling time, the powder was continually deformed and work hardening effects became severe, and as a result, the as-milled powder started to become fractured [39]. This explains the phenomenon that the as-milled powder particle size is slightly reduced after 10 h milling compared to that of the powder milled after 5 h [40]. By further increasing the milling time, the fracture phenomenon of the as-milled powders takes a more important role than the cold welding effect, and this leads to the particle size of the as-milled powders continually decreasing [39]. Due to the increased fracturing, during the final phases of milling the powder yield increased as a function of milling time. Although HEA is formed at 5 h of milling, it is nevertheless highly beneficial to mill for 20 h in order to guarantee a high powder yield (97%) and finer particles, which results in a high driving force during the sintering stage. Hence, a 20 h as-milled powder was utilized for further investigation and consolidation.

3.4. Thermogravimetric Analysis

Figure 4 represents the DSC curve of the 20 h as-milled HEA NiMnFeCu powder. It can be seen that the powder had both exothermic and endothermic trends. There are three endothermic peaks, which are at 77 °C, 1066 °C, and 1220 °C.

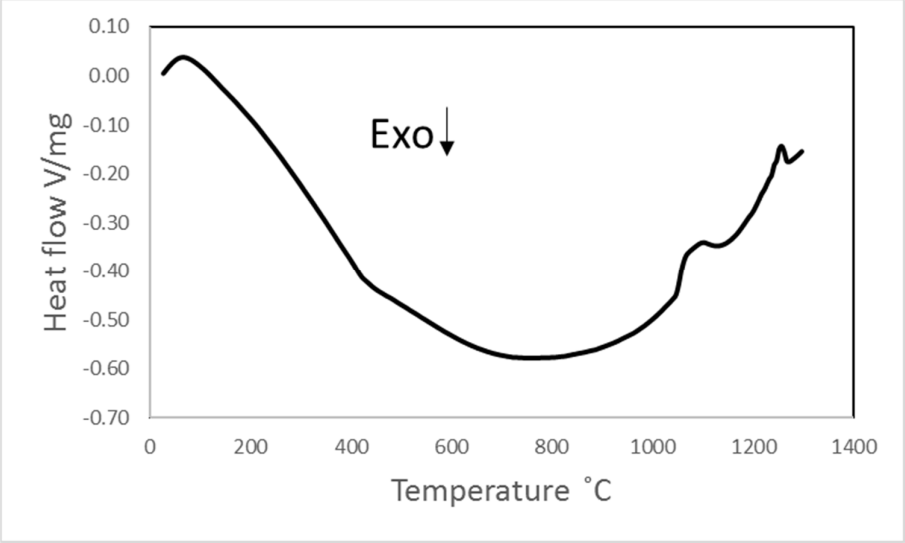

Figure 4. DSC curve of the as-milled NiMnFeCu HEA after 20 h of milling.

The endothermic peak at 77 °C corresponds to decomposition and volatilisation of the process control agent (viz, ethanol). Since the as-milled powders contain a large amount of internal stress that is induced by work hardening and plastic deformation, the exothermic zone up to 800 °C corresponded to the internal stress relieving stage during heating [41]. The broad endothermic range between 1060 °C and 1080 °C could be related to the presence of a partial liquid phase due to rapid absorption of energy prior to complete melting [42,43]. The sharp endothermic peak at 1220 °C suggests that the HEA powder is completely molten at this stage and also that this temperature is very close to the theoretical melting point of the NiMnFeCu HEA powder (1331 °C). Based on this analysis, two sintering temperatures are selected for consolidating the as-milled HEA NiMnFeCu alloy powders, which are 1000 °C (in the complete solid region) and 1050 °C (in the presence of a partial liquid phase). The sintering conditions and the detailed fabricated materials information are summarised in Table 3.

Table 3. Pore size and morphology of the as-sintered HEA NiMnFeCu under various conditions.

Sample	Temperature (°C)	Time (h)	Average Pore Size (μm)	Circularity of Pores Index	Relative Sintered Density (%)
S1	1000	1	34.78	0.41	79
S2	1000	2	37.356	0.46	82
S3	1050	1	11.2	0.872	80
S4	1050	2	8.1	0.890	98

3.5. Effect of Sintering Temperature Conditions

Figure 5 shows the XRD patterns of the as-sintered NiMnFeCu under various sintering conditions (S1–S4). Table 3 summarises the details of the sintering conditions. It is clearly seen that the as-sintered alloys (S1–S4) at all conditions consist of a single FCC HEA phase. This suggests that during the sintering process, no phase transformation takes place.

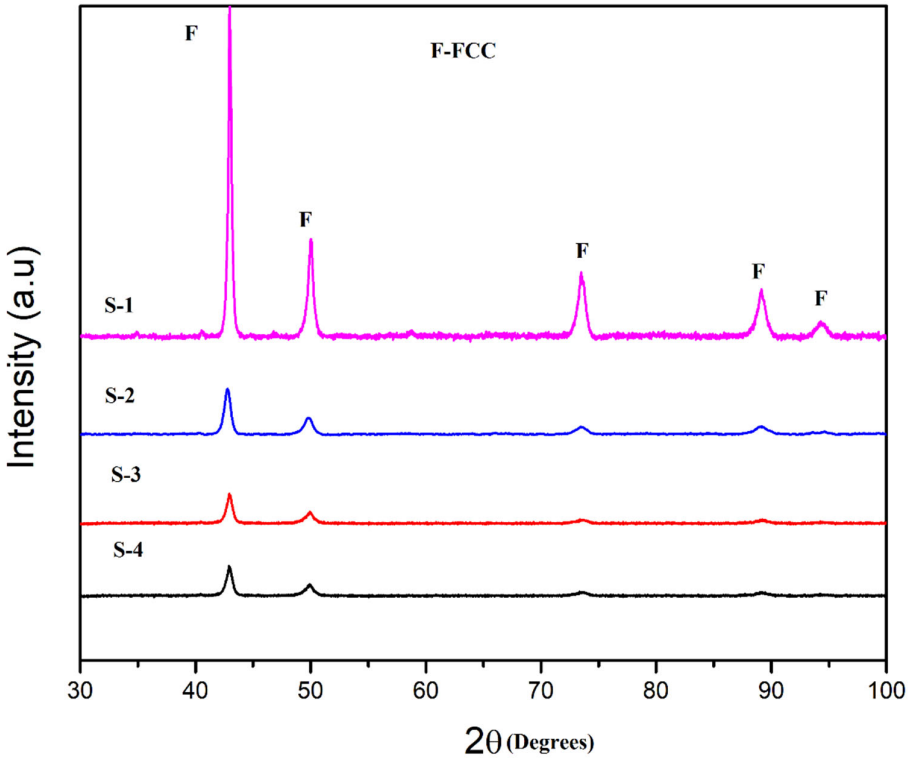

Figure 5. XRD patterns of as-sintered HEA NiMnFeCu at various sintering conditions.

Figures 6 and 7 show the microstructure of the as-sintered HEA under low and high magnification as a result of the various sintering conditions. It is evident that the microstructure of S1 and S2 samples were porous. The morphology of the pores was irregular. In S1, the pores were spaced very close to each other, while in S2 the pores were clustered in a few areas of the microstructure. In case of condition S3, a significant number of pores was seen, however the morphology of the pores was spherical. The condition S4 had negligible pores and was observed only under high magnification. Careful observation of the microstructure under high magnification using Figure 7a–d showed that the black shades were surrounded by a grey matrix. The black shades correspond to pores while the grey matrix corresponds to the HEA. The grey matrix was homogenous throughout the microstructure and no secondary phases were found. Hence, it can be concluded that the HEA NiMnFeCu has formed a random solid solution with FCC crystal structure under all sintering conditions.

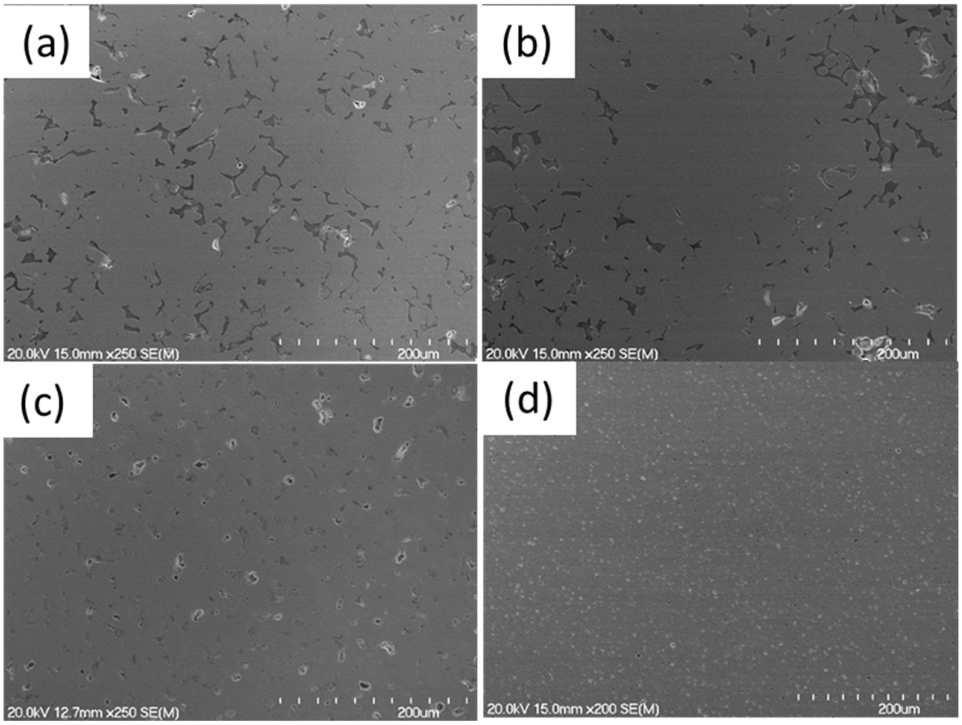

Figure 6. SEM images of the as-sintered NiMnFeCu under low magnification. (**a**) At 1000 °C for 1 h (S1), (**b**) at 1000 °C for 2 h (S2), (**c**) at 1050 °C for 1 h (S3), (**d**) at 1050 °C for 2 h (S4).

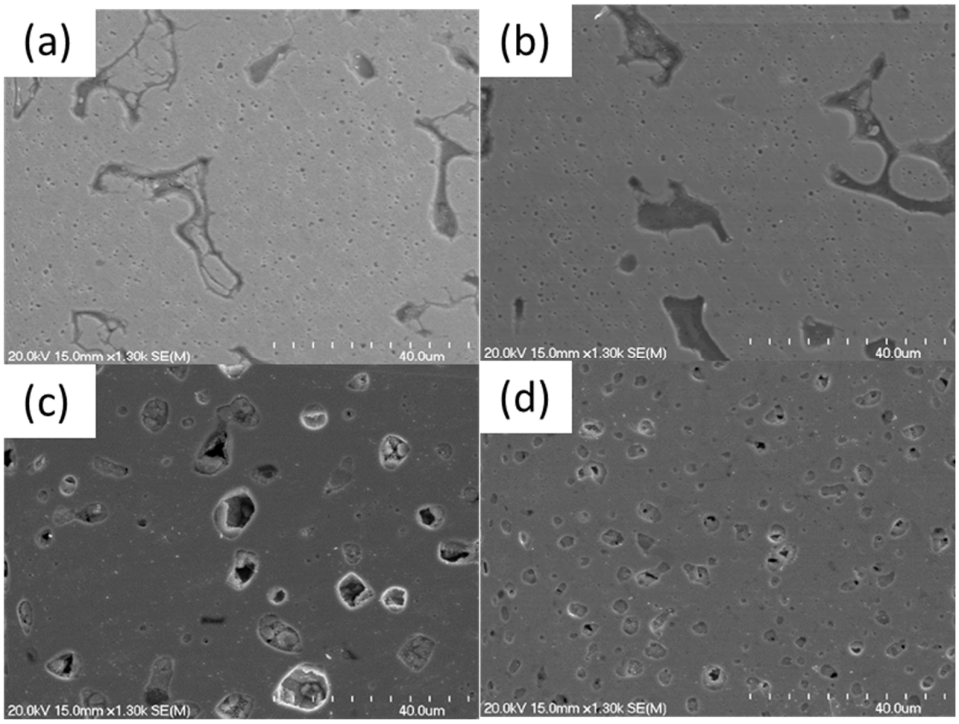

Figure 7. SEM images of the as sintered HEA NiMnFeCu at high magnification. (**a**) At 1000 °C for 1 h (S1), (**b**) at 1000 °C for 2 h (S2), (**c**) at 1050 °C for 1 h (S3), (**d**) at 1050 °C for 2 h (S4).

Figure 8 shows the SEM/EDS elemental mapping of the as-milled NiMnFeCu powders at 20 h and the as-sintered NiMnFeCu HEA under the condition S2. It is clearly seen that the NiMnFeCu HEA has formed a single phase random solid solution with good

chemical homogeneity in both the as-milled and the as-sintered state. Table 4 summarises the measured weight percentages of the constituent elements of the as-milled NiMnFeCu HEA powders at 20 h and the as-sintered NiMnFeCu HEA under condition S2 (full area scan of Figure 8). It is clearly observed that the measured weight percentages of the elements were very close to the nominal weight percentages in the as-milled and as-sintered states.

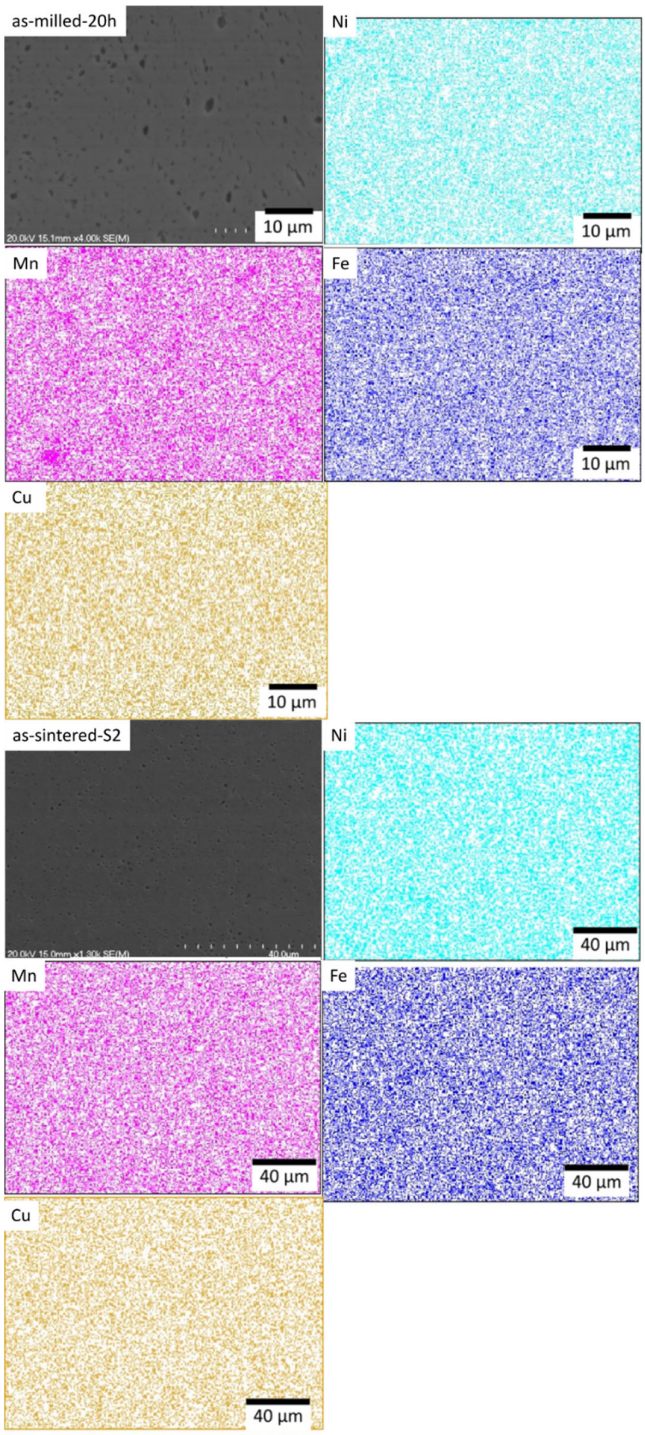

Figure 8. SEM/EDS mapping of the as-milled NiMnFECu powders at 20 h and as-sintered NiMnFeCu alloy at conditions S2 (sintering at 1000 °C for 2 h).

Table 4. Comparison of nominal and measured weight proportion of the as-milled and the as-sintered NiMnFeCu.

Elements	Ni	Fe	Mn	Cu
Nominal weight %	25.2	23.9	23.6	27.2
As-milled measured weight% (Area scan) 20 h	27.03	24.99	24.49	22.14
As-sintered measured (S2) weight% (Area scan)	25.36	26.18	25.90	22.56

Figure 9 shows the OM micrographs of the as-sintered NiMnFeCu at various sintering conditions. It is seen that the S1–S3 alloys are porous. The information regarding the pore size and the morphology for the sintered NiMnFeCu HEAs (S1–S4) are summarised in Table 3. The average pore sizes of S1 and S2 were 34.7 μm and 37.3 μm, respectively, and the morphology of the pores of S1 and S2 remained irregular. The average pore sizes of S3 and S4 were 11.2 μm and 8.1 μm, respectively. The morphology of the pores of S3 and S4 changed to spherical. The sintered relative densities of S1 and S2 were 79% and 82%, respectively, and the sintered relative density values of S3 and S4 were 80% and 98%, respectively.

The microstructures of S1–S3 had many pores present, and the relative density for those three samples are much lower than that of S4. For S1 and S2, the sintering temperature was relatively low (1000 °C) compared to S3 (1050 °C), the sintering time is 1 h for S1 and S3 and 2 h for S2 and S4. From the microstructure observation (Figure 7), limited densification takes place for the S1–S3 samples, and large densification happened for the S4 sample. The microstructure of S4 has negligible pores, and S4 has a relative density of 98%. This enhanced densification is due to the existence of a small portion of liquid phase and sufficient sintering time and optimum temperature [43]. A partial liquid phase exists at conditions S3 and S4, and as a result, the morphology of the pores in these samples is spherical. However maximum densification takes place only for S4, because S4 has a longer sintering time compared to S3. Prolonging the sintering time in the presence of a partial liquid phase aided the sintering by spreading and wetting the solid particles through capillary action, thereby the pores became filled and the final sintered density increased [44].

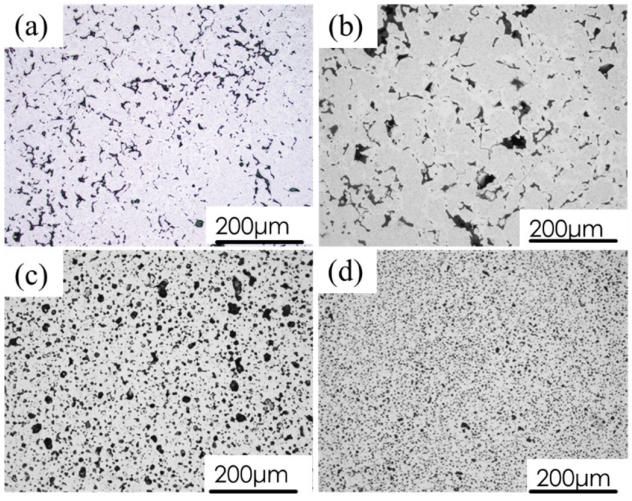

Figure 9. OM micrographs of as-sintered HEA NiMnFeCu. (**a**) At 1000 °C for 1 h (S1), (**b**) at 1000 °C for 2 h (S2), (**c**) at 1050 °C for 1 h (S3), (**d**) at 1050 °C for 2 h (S4).

3.5.1. Micro-Hardness

Figure 10 depicts the mean and standard deviation of micro-hardness measurements of NiMnFeCu HEA under sintering conditions S1–S4. It can be seen that the micro-hardness of HEA made under condition S4 is higher when compared to those HEAs made under conditions S1–S3. The mean and standard deviation of micro-hardness of S1 and S2 were 104.88 ± 9 Hv and 198.79 ± 8 Hv, respectively, and for S3 and S4 the micro-hardness values were 115.28 ± 7 HV and 233.45 ± 9 HV, respectively.

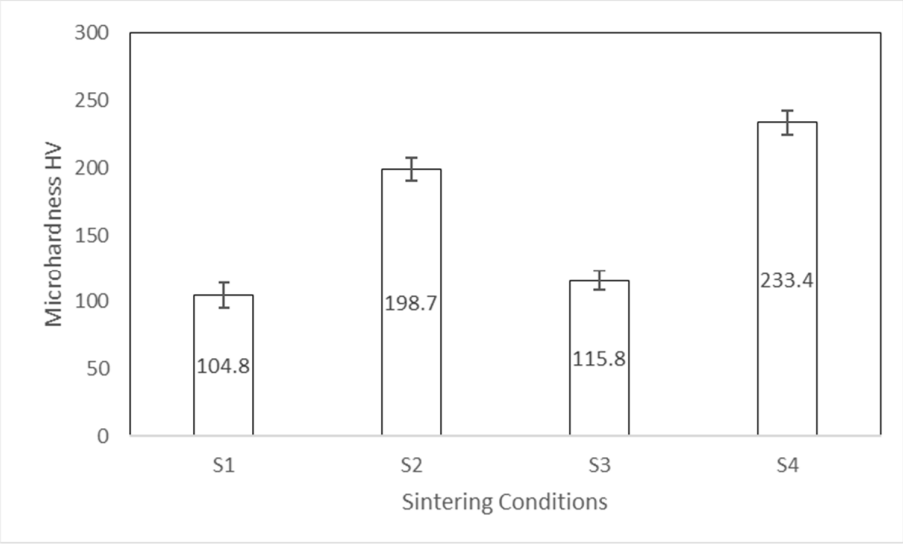

Figure 10. Micro-hardness tests of as sintered NiMnFeCu under various sintering conditions.

Based on the microstructural characterization above (Figure 9), S4 has negligible porosity and high relative sintered density when compared to other sintering conditions (S1–S3). As a result, the micro-hardness of S4 is significantly higher when compared to S1–S3. The presence of a high residual porosity and low relative sintered density leads to the low micro-hardness of samples S1–S3. For the samples S2 and S3, the relative sintered density is very close to each other, however the micro-hardness value of S2 is significantly higher than S3. It has been reported elsewhere that along with the density, the spatial and topological distribution of pores also plays a critical role in the mechanical properties of the fabricated material [45,46]. Since the depth of penetration of micro-hardness tested even at maximum load (9.80 N) is only a few μm, the influence of topological distribution (along the depth) of pores can be neglected while the spatial distribution (along the length and width) of the pores can be taken in account. The micro-hardness of S2 is higher compared to S3 because the microstructure of S2 had pores distributed in clusters and they were spaced wider from each other while the pores in S3 were distributed very closely to each other, hence there is more probability for a pore to be present directly below the indent. As a result, the micro-hardness values of S3 were lower compared to S2 [45].

NiMnFeCu retained its single-phase FCC crystal structure under all sintering conditions (S1–S4). The most reported single-phase FCC HEAs possess hardness values ranging from 100 to 200 HV [2,47]. Hence, the as-sintered NiMnFeCu at condition S4 possessed micro-hardness comparable to that of other single-phase FCC HEAs listed in Table 5.

Table 5. Micro-hardness of 3D transition metal based HEAs reported from the literature.

HEA	Micro-Hardness HV	Reference
Al0.25CoFeNi	138	[47]
CoFeNiSi0.25	149	[48]
CoCrFeNi	116	[47]
NiMnFeCu	233.4	Present work

3.5.2. Compression

Figure 11 shows the compressive yield stress of the as-sintered NiMnFeCu under various sintering conditions. It appeared evident that the condition S4 possessed greater yield strength when compared to all other sintering conditions (S1–S3). For the conditions S1 and S2, the alloy yielded at 298.7 MPa and 389.8 MPa, respectively, and for S3 and S4 the alloys possessed a yield stress of 295.9 MPa and 516.3 MPa, respectively.

S4 possessed better yield strength when compared to all other alloys (S1–S3) because of its high final sintered density and less porosity. The microstructures of S1–S3 contain high porosity, and this leads to reduction in yield strength. Despite the similar relative densities of the samples S2 and S3, their compressive yield strength varied significantly with each other. This could be attributed to the spatial distribution of pores [45]. Along with density/porosity, the grain size will also affect the mechanical properties (hardness/yield stress). However, the effect of grain size on mechanical properties is beyond the scope of this research paper and it will be studied in future using advanced characterization techniques such as EBSD. The studied NiMnFeCu (S4) possessed superior compressive yield strength when compared to other 3d transition metal based HEAs listed in Table 6. Due to the permissible structural properties of the alloy NiMnFeCu under conditions S2 and S4, they could be considered as a promising self-supported electrocatalyst for industrial water electrolysis applications. Therefore, S2 and S4 were selected to perform preliminary electrochemical studies, intended for water electrolysis applications.

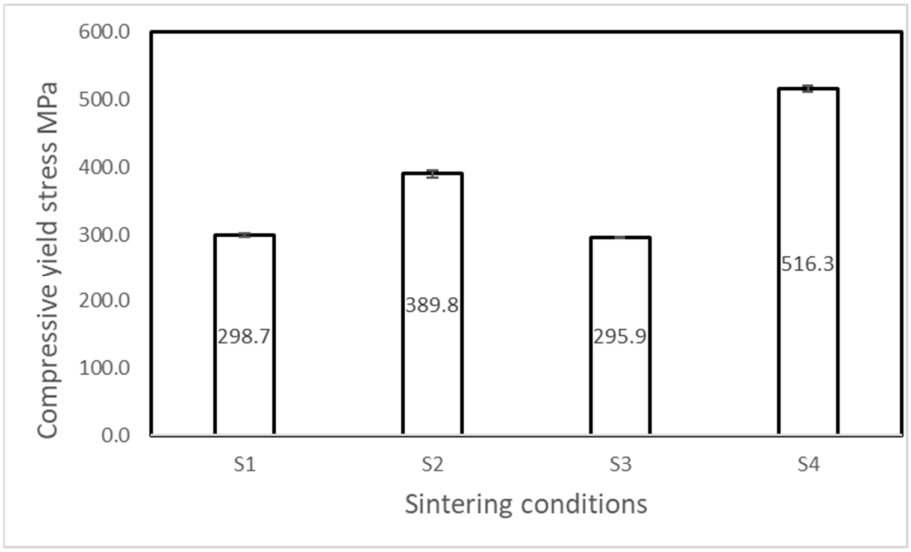

Figure 11. Compressive yield stress of the as-sintered HEA NiMnFeCu under various sintering conditions.

Table 6. Compressive yield stress of 3d transition metal based HEAs reported in the literature.

HEA	Compressive Yield Stress MPA	Reference
Al0.25CoFeNi	158	[47]
CoFeNiSi0.25	196	[48]
CoCrFeNi	148	[47]
NiMnFeCu	516.3	Present work

3.6. Electrocatalysis of Oxygen Evolution Reaction

Figure 12a shows the linear sweep voltammetry (LSV) curve of the as-sintered NiMnFeCu alloy under various conditions at a scan rate of 5 mVs^{-1} and Figure 12b shows the Tafel slope of the as-sintered NiMnFeCu alloy under various conditions. Figure 12c depicts the chronoamperometry curve of the as-sintered NiMnFeCu (S2) at a constant potential of 1.7 V (vs. RHE). The catalytic activity of the alloy is estimated through the LSV curve, as it measures the overpotential of the oxygen evolution reactions (OER). The onset potential is the potential where the current density increases sharply in the LSV spectra. The onset overpotential of S2 with CV 100 cycles, S2 and S4 were 310 mV, 340 mV and 410 mV, respectively. To reach the current density of 10 mA cm^{-2}, the as-sintered NiMnFeCu under conditions S2 with CV 100 cycles, S2 and S4 require an overpotential of 322 mV, 362 mV and 438 mV (E(RHE)−1.23 V), respectively, and their corresponding Tafel slopes were measured to be 113 mV/dec, 157 mV/dec, and 160 mV/dec, respectively. The stability of the as-sintered NiMnFeCu alloy (S2) was analysed using a chronoamperometry curve and the electrode measured a current density of 48 mA cm^{-2} initially, and at the end of 10 h the current density was 39 mA cm^{-2} , hence the electrocatalyst showed a minimum change in current density and retained 64% of current density for 10 h.

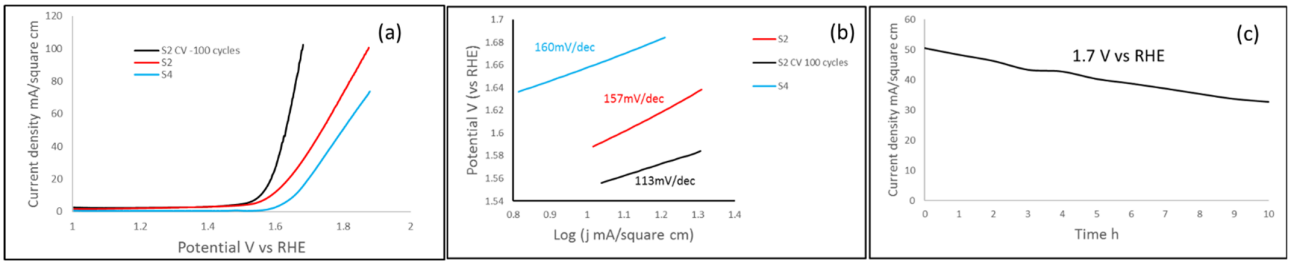

Figure 12. Electrochemical characterization of the as-sintered NiMnFeCu at various sintering conditions. (**a**) Linear sweep voltammetry curve at the scan rate of 5 mV s^{-1}, (**b**) Tafel slopes derived from LSV curves, (**c**) chronoamperometry curve of the as-sintered NiMnFeCu (S2) at constant potential 1.7 V (vs. RHE).

The HEA NiMnFeCu under condition S2 with CV 100 cycles showed a relatively lower overpotential of 322 mV for reaching the current density of 10 mA cm^{-2} when compared to HEA alloys under conditions S2 and S4. This lower overpotential implies that lower energy is required to initiate the surface adsorption and desorption reactions of intermediates on the electrode. Hence, the comparatively better catalytic activity of S2 with 100 cycles of CV could be due to the presence of porous microstructure and the formation of nano oxide sheets during the cyclic voltammetry sweep. The combination of porosity and nano oxide layers exposed the active sites and enhanced the catalytic activity [24,25]. So, the overpotential of S2 is lower when compared to S4, but not as low as S2-CV 100 cycles because of the presence of porosity and the absence of nano oxide layers. The condition S4 had negligible porosity and no nano oxide layer, so its overpotential was relatively higher when compared to all the other studied conditions. In addition to that, the merit of a catalyst is also defined by the Tafel slope, with a smaller Tafel slope implying faster OER kinetics, hence for condition S2-CV 100 cycles, the Tafel slope was the smallest among the other studied conditions. The faster kinetics is due to porosity and nano oxide layers formed on the surface of the catalyst. The catalytic activity of the self-supported HEA electrocatalyst at conditions S2- CV 100 cycles was comparable to the existing state-of-the-art electrocatalysts IrO_2 (η = 410 mV @ 0.5 M KOH) and RuO_2 (η = 358 mV @ 0.5 M KOH) [21]. The group VIII 3D metals in mono-metallic form or in their corresponding phosphides, selenides, and sulphides are widely used as electrocatalysts for OER reactions [49]. In mono-metallic form Ni (η = 444 mV @ 10 mA cm^{-2}) [50], Mn (η = 540 mV @ 10 mA cm^{-2}) [51], Fe (η = 420 mV @ 10 mA cm^{-2}) [52], and Cu (η = 525 mV @ 1 mA cm^{-2})

[53] showed modest catalytic activity. However, in multi-metallic form (HEA NiMnFeCu) the catalytic activity improved drastically. In order to explore the origins of the excellent electrocatalytic properties in multi-metallic materials, researchers have claimed that optimum bonding strength (neither too strong or neither too weak) between the electrodes and the intermediates is required (the Sabatier principle) [54]. The d-band vacancy (d-electron count) is the widely accepted descriptor for determining the bonding strength. Multi metallic alloys provide a better opportunity to fine tune the d-band vacancy when compared to mono metallic materials. Hence, there is increased OER kinetics in multi-metallic materials such as HEAs. In addition to that, it has been widely speculated that the existence of synergy among the alloying elements in HEAs (the cocktail effect) could also contribute to the excellent catalytic activity, although more clarity is required in explaining this effect [27,28]. The overpotential of the alloy under the conditions S2-CV 100 cycles are comparable to the most reported HEAs in the literature such as MnFeCoNi (η = 302 mV) and CoCrFeNiMo (η = 220 mV) [24,27,31]. It is worth noting that the OER activity of the as-sintered NiMnFeCu was directly measured from the bulk alloy with less active sites when compared to the nanostructured 2D catalyst, which are often grafted onto a support such as carbon fibre paper or nickel foams. Hence, the catalytic activity is the intrinsic property of the as-sintered NiMnFeCu HEA, which could be due to the unique properties such as synergistic effects and compositional randomness. Bulk NiMnFeCu under condition S2 with CV 100 cycles has excellent mechanical properties and good electrochemical properties, Hence, it could be used as a potential self-supported electrocatalyst for industrial scale water electrolysis.

4. Conclusions

A single-phase face centred NiMnFeCu HEA was successfully synthesised using the combined techniques of MA and vacuum sintering. Under the sintering conditions S2 and S4, the alloy possessed relative sintered density of about 82% and 98%, respectively, and the alloy showed acceptable mechanical properties with a yield strength of 389.8 MPa and 516.3 MPa, respectively. In addition, micro-hardness values were measured to be 198.79 ± 8 Hv and 233.45 ± 9 HV, respectively. Preliminary electrochemical studies showed that the alloy S2 with CV 100 cycles requires an overpotential of 322 mV to reach a current density of 10 mA cm^{-2}. The favourable catalytic activity observed is due to the porous microstructure and formation of nano oxide layers. The alloy S2 showed modest catalytic activity due to its porous structure but no nano oxide layer was present. S4 showed relatively poor catalytic activity due to the absence of porosity and nano oxide layers. Chronoamperometry analysis showed that the alloy S2 showed excellent stability with minimum change in current density at a constant potential of 1.7 V vs. (RHE) for 10 h with a current retention of 64%. Hence, HEA NiMnFeCu under condition S2 possesses permissible structural properties and good electrochemical properties on the CV sweep, hence they can be employed in industrial scale water electrolysis. Furthermore, fine tuning of d band vacancies will be further explored by means of theoretical calculations such as density function theory. X-ray photoelectron spectroscopy (XPS) will be employed to analyse the surface characteristics of the electrode in future investigations.

Author Contributions: A.K.: Writing—original draft, investigation, formal analysis; M.M.: writing—review and editing, supervision; L.B.: methodology, supervision; Y.M.L.: methodology; F.K.: methodology, resource; F.Y.: conceptualization, methodology, investigation, writing—review and editing, supervision. All authors have read and agreed to the published version of the manuscript.

Funding: This research is funded by National Nature Science Foundation of China (Project No. 51971074).

Data Availability Statement: The data presented in this study are available upon request from the corresponding author.

Conflicts of Interest: The authors declare no conflict of interest.

Reference

1. Cheng, C.-Y.; Yang, Y.-C.; Zhong, Y.-Z.; Chen, Y.-Y.; Hsu, T.; Yeh, J.-W. Physical metallurgy of concentrated solid solutions from low-entropy to high-entropy alloys. *Curr. Opin. Solid State Mater. Sci.* **2017**, *21*, 299–311. https://doi.org/10.1016/j.cossms.2017.09.002.
2. Miracle, D.B.; Senkov, O.N. A critical review of high entropy alloys and related concepts. *Acta Mater.* **2017**, *122*, 448–511. https://doi.org/10.1016/j.actamat.2016.08.081.
3. Tsai, M.-H.; Yeh, J.-W. High-entropy alloys: A critical review. *Mater. Res. Lett.* **2014**, *2*, 107–123.
4. Yeh, J.-W.; Chen, S.K.; Lin, S.-J.; Gan, J.-Y.; Chin, T.-S.; Shun, T.-T.; Tsau, C.-H.; Chang, S.-Y. Nanostructured High-Entropy Alloys with Multiple Principal Elements: Novel Alloy Design Concepts and Outcomes. *Adv. Eng. Mater.* **2004**, *6*, 299–303. https://doi.org/10.1002/adem.200300567.
5. Cantor, B.; Chang, I.T.H.; Knight, P.; Vincent, A.J.B. Microstructural development in equiatomic multicomponent alloys. *Mater. Sci. Eng. A* **2004**, *375–377*, 213–218. https://doi.org/10.1016/j.msea.2003.10.257.
6. Cao, Y.; Liu, Y.; Liu, B.; Zhang, W. Precipitation behavior during hot deformation of powder metallurgy Ti-Nb-Ta-Zr-Al high entropy alloys. *Intermetallics* **2018**, *100*, 95–103. https://doi.org/10.1016/j.intermet.2018.06.007.
7. Chen, S.-T.; Tang, W.-Y.; Kuo,Y.-F.; Chen, S.-Y.; Tsau, C.-H.; Shun, T.-T.; Yeh, J.-W. Microstructure and properties of age-hardenable AlxCrFe1. 5MnNi0. 5 alloys. *Mater. Sci. Eng. A* **2010**, *527*, 5818–5825.
8. Li, Q.; Zhang, H.; Li, D.; Chen, Z.; Huang, S.; Lu, Z.; Yan, H. WxNbMoTa Refractory High-Entropy Alloys Fabricated by Laser Cladding Deposition. *Materials* **2019**, *12*, 533. https://doi.org/10.3390/ma12030533.
9. Raza, A.; Kang, B.; Lee, J.; Ryu, H.J.; Hong, S.H. Transition in microstructural and mechanical behavior by reduction of sigma-forming element content in a novel high entropy alloy. *Mater. Des.* **2018**, *145*, 11–19. https://doi.org/10.1016/j.matdes.2018.02.036.
10. Raza, A.; Ryu, H.J.; Hong, S.H. Strength enhancement and density reduction by the addition of Al in CrFeMoV based high-entropy alloy fabricated through powder metallurgy. *Mater. Des.* **2018**, *157*, 97–104. https://doi.org/10.1016/j.matdes.2018.07.023.
11. Chuang, M.-H.; Tsai, M.-H.; Wang, W.-R.; Lin, S.-J.; Yeh, J.-W. Microstructure and wear behavior of AlxCo1.5CrFeNi1.5Tiy high-entropy alloys. *Acta Mater.* **2011**, *59*, 6308–6317. https://doi.org/10.1016/j.actamat.2011.06.041.
12. Wu, J.-M.; Lin, S.-J.; Yeh, J.-W.; Chen, S.-K.; Huang, Y.-S.; Chen, H.-C. Adhesive wear behavior of AlxCoCrCuFeNi high-entropy alloys as a function of aluminum content. *Wear* **2006**, *261*, 513–519. https://doi.org/10.1016/j.wear.2005.12.008.
13. Hsu, C.-Y.; Yeh, J.-W.; Chen, S.-K.; Shun, T.-T. Wear resistance and high-temperature compression strength of Fcc CuCoNiCrAl0.5Fe alloy with boron addition. *Met. Mater. Trans. A* **2004**, *35*, 1465–1469. https://doi.org/10.1007/s11661-004-0254-x.
14. Hemphill, M.; Yuan, T.; Wang, G.; Yeh, J.; Tsai, C.; Chuang, A.; Liaw, P. Fatigue behavior of Al0.5CoCrCuFeNi high entropy alloys. *Acta Mater.* **2012**, *60*, 5723–5734. https://doi.org/10.1016/j.actamat.2012.06.046.
15. Seifi, M.; Li, D.; Yong, Z.; Liaw, P.K.; Lewandowski, J. Fracture Toughness and Fatigue Crack Growth Behavior of As-Cast High-Entropy Alloys. *JOM* **2015**, *67*, 2288–2295. https://doi.org/10.1007/s11837-015-1563-9.
16. Tang, Z.; Gao, M.C.; Diao, H.; Yang, T.; Liu, J.; Zuo, T.; Zhang, Y.; Lu, Z.; Cheng, Y.; Zhang, Y.; et al. Aluminum Alloying Effects on Lattice Types, Microstructures, and Mechanical Behavior of High-Entropy Alloys Systems. *JOM* **2013**, *65*, 1848–1858. https://doi.org/10.1007/s11837-013-0776-z.
17. Xiao, D.H.; Zhou, P.F.; Wu, W.Q.; Diao, H.Y.; Gao, M.C.; Song, M.; Liaw, P.K. Microstructure, mechanical and corrosion behaviors of AlCoCuFeNi-(Cr, Ti) high entropy alloys. *Mater. Des.* **2017**, *116*, 438–447.
18. Sekhar, R.A.; Samal, S.; Nayan, N.; Bakshi, S.R. Microstructure and mechanical properties of Ti-Al-Ni-Co-Fe based high entropy alloys prepared by powder metallurgy route. *J. Alloy. Compd.* **2019**, *787*, 123–132. https://doi.org/10.1016/j.jallcom.2019.02.083.
19. Yu, F.; Yu, L.; Mishra, I.; Yu, Y.; Ren, Z.; Zhou, H. Recent developments in earth-abundant and non-noble electrocatalysts for water electrolysis. *Mater. Today Phys.* **2018**, *7*, 121–138. https://doi.org/10.1016/j.mtphys.2018.11.007.
20. Song, F.; Bai, L.; Moysiadou, A.; Lee, S.; Hu, C.; Liardet, L.; Hu, X. Transition Metal Oxides as Electrocatalysts for the Oxygen Evolution Reaction in Alkaline Solutions: An Application-Inspired Renaissance. *J. Am. Chem. Soc.* **2018**, *140*, 7748–7759. https://doi.org/10.1021/jacs.8b04546.
21. Suen, N.-T.; Hung, S.-F.; Quan, Q.; Zhang, N.; Xu, Y.-J.; Chen, H.M. Electrocatalysis for the oxygen evolution reaction: Recent development and future perspectives. *Chem. Soc. Rev.* **2017**, *46*, 337–365. https://doi.org/10.1039/c6cs00328a.
22. Carrette, L.; Friedrich, K.A.; Stimming, U. Fuel cells–fundamentals and applications. *Fuel Cells* **2001**, *1*, 5–39.
23. Cai, Z.-X.; Goou, H.; Ito, Y.; Tokunaga, T.; Miyauchi, M.; Abe, H.; Fujita, T. Nanoporous ultra-high-entropy alloys containing fourteen elements for water splitting electrocatalysis. *Chem. Sci.* **2021**, *12*, 11306–11315. https://doi.org/10.1039/d1sc01981c.
24. Dai, W.; Lu, T.; Pan, Y. Novel and promising electrocatalyst for oxygen evolution reaction based on MnFeCoNi high entropy alloy. *J. Power Sources* **2019**, *430*, 104–111. https://doi.org/10.1016/j.jpowsour.2019.05.030.
25. Tang, J.; Xu, J.; Ye, Z.; Li, X.; Luo, J. Microwave sintered porous CoCrFeNiMo high entropy alloy as an efficient electrocatalyst for alkaline oxygen evolution reaction. *J. Mater. Sci. Technol.* **2021**, *79*, 171–177. https://doi.org/10.1016/j.jmst.2020.10.079.
26. Ma, P.; Zhao, M.; Zhang, L.; Wang, H.; Gu, J.; Sun, Y.; Ji, W.; Fu, Z. Self- supported high-entropy alloy electrocatalyst for highly efficient H2 evolution in acid condition. *J. Mater.* **2020**, *6*, 736–742. https://doi.org/10.1016/j.jmat.2020.06.001.

27. Cui, X.; Zhang, B.; Zeng, C.; Guo, S. Electrocatalytic activity of high-entropy alloys toward oxygen evolution reaction. *MRS Commun.* **2018**, *8*, 1230–1235. https://doi.org/10.1557/mrc.2018.111.
28. Zhang, G.; Ming, K.; Kang, J.; Huang, Q.; Zhang, Z.; Zheng, X.; Bi, X. High entropy alloy as a highly active and stable electrocatalyst for hydrogen evolution reaction. *Electrochim. Acta* **2018**, *279*, 19–23. https://doi.org/10.1016/j.electacta.2018.05.035.
29. Gao, S.; Hao, S.; Huang, Z.; Yuan, Y.; Han, S.; Lei, L.; Zhang, X.; Shahbazian-Yassar, R.; Lu, J. Synthesis of high-entropy alloy nanoparticles on supports by the fast moving bed pyrolysis. *Nat. Commun.* **2020**, *11*, 1–11. https://doi.org/10.1038/s41467-020-15934-1.
30. Huang, J.; Du, K.; Wang, P.; Yin, H.; Wang, D. Electrochemical preparation and homogenization of face-centered FeCoNiCu medium entropy alloy electrodes enabling oxygen evolution reactions. *Electrochim. Acta* **2021**, *378*, 138142. https://doi.org/10.1016/j.electacta.2021.138142.
31. Jia, Z.; Yang, T.; Sun, L.; Zhao, Y.; Li, W.; Luan, J.; Lyu, F.; Zhang, L.-C.; Kruzic, J.J.; Kai, J.-J.; et al. A novel multinary intermetallic as an active electrocatalyst for hydrogen evolution. *Adv. Mater.* **2020**, *32*, 2000385.
32. Kang, B.; Lee, J.; Ryu, H.J.; Hong, S.H. Ultra-high strength WNbMoTaV high-entropy alloys with fine grain structure fabricated by powder metallurgical process. *Mater. Sci. Eng. A* **2018**, *712*, 616–624. https://doi.org/10.1016/j.msea.2017.12.021.
33. Takeuchi, A.; Inoue, A. Classification of Bulk Metallic Glasses by Atomic Size Difference, Heat of Mixing and Period of Constituent Elements and Its Application to Characterization of the Main Alloying Element. *Mater. Trans.* **2005**, *46*, 2817–2829. https://doi.org/10.2320/matertrans.46.2817.
34. Zhang, Y.; Lu, Z.P.; Ma, S.G.; Liaw, P.K.; Tang, Z.; Cheng, Y.Q.; Gao, M.C. Guidelines in predicting phase formation of high-entropy alloys. *MRS Commun.* **2014**, *4*, 57–62. https://doi.org/10.1557/mrc.2014.11.
35. Guo, S.; Ng, C.; Lu, J.; Liu, C.T. Effect of valence electron concentration on stability of fcc or bcc phase in high entropy alloys. *J. Appl. Phys.* **2011**, *109*, 103505. https://doi.org/10.1063/1.3587228.
36. Hong, W.T.; Welsch, R.E.; Shao-Horn, Y. Descriptors of Oxygen-Evolution Activity for Oxides: A Statistical Evaluation. *J. Phys. Chem. C* **2016**, *120*, 78–86. https://doi.org/10.1021/acs.jpcc.5b10071.
37. Garlapati, M.M.; Vaidya, M.; Karati, A.; Mishra, S.; Bhattacharya, R.; Murtya, B.S. Influence of Al content on thermal stability of nanocrystalline AlxCoCrFeNi high entropy alloys at low and intermediate temperatures. *Adv. Powder Technol.* **2020**, *31*, 1985–1993.
38. Ren, B.; Liu, Z.; Li, D.; Shi, L.; Cai, B.; Wang, M. Effect of elemental interaction on microstructure of CuCrFeNiMn high entropy alloy system. *J. Alloy. Compd.* **2010**, *493*, 148–153. https://doi.org/10.1016/j.jallcom.2009.12.183.
39. Wang, G.; Liu, Q.; Yang, J.; Li, X.; Sui, X.; Gu, Y.; Liu, Y. Synthesis and thermal stability of a nanocrystalline MoNbTaTiV refractory high-entropy alloy via mechanical alloying. *Int. J. Refract. Met. Hard Mater.* **2019**, *84*, 104988. https://doi.org/10.1016/j.ijrmhm.2019.104988.
40. Suryanarayana, C. Mechanical alloying and milling. *Prog. Mater. Sci.* **2001**, *46*, 1–184.
41. Ji, W.; Fu, Z.; Wang, W.; Wang, H.; Zhang, J.; Wang, Y.; Zhang, F. Mechanical alloying synthesis and spark plasma sintering consolidation of CoCrFeNiAl high-entropy alloy. *J. Alloy. Compd.* **2014**, *589*, 61–66. https://doi.org/10.1016/j.jallcom.2013.11.146.
42. Cheng, H.; Xie, Y.-C.; Tang, Q.-H.; Rao, C.; Dai, P.-Q. Microstructure and mechanical properties of FeCoCrNiMn high-entropy alloy produced by mechanical alloying and vacuum hot pressing sintering. *Trans. Nonferrous Met. Soc. China* **2018**, *28*, 1360–1367. https://doi.org/10.1016/s1003-6326(18)64774-0.
43. Rohila, S.; Mane, R.B.; Ummethala, G.; Panigrahi, B.B. Nearly full-density pressureless sintering of AlCoCrFeNi-based high-entropy alloy powders. *J. Mater. Res.* **2019**, *34*, 777–786.
44. Calderon, R.D.O.; Gierl-Mayer, C.; Danninger, H. Fundamentals of Sintering: Liquid Phase Sintering. In *Encyclopedia of Materials: Metals and Alloys*; Elsevier: Oxford, UK, 2022; pp. 481–492.
45. Venkataraman, R.; Das, G.; Singh, S.; Pathak, L.; Ghosh, R.; Krishnamurthy, R. Study on influence of porosity, pore size, spatial and topological distribution of pores on microhardness of as plasma sprayed ceramic coatings. *Mater. Sci. Eng. A* **2007**, *445–446*, 269–274. https://doi.org/10.1016/j.msea.2006.09.042.
46. Bilger, N.; Auslender, F.; Bornert, M.; Michel, J.-C.; Moulinec, H.; Suquet, P.; Zaoui, A. Effect of a nonuniform distribution of voids on the plastic response of voided materials: A computational and statistical analysis. *Int. J. Solids Struct.* **2005**, *42*, 517–538. https://doi.org/10.1016/j.ijsolstr.2004.06.048.
47. Gorsse, S.; Nguyen, M.H.; Senkov, O.N.; Miracle, D.B. Database on the mechanical properties of high entropy alloys and complex concentrated alloys. *Data Brief.* **2018**, *21*, 2664–2678. https://doi.org/10.1016/j.dib.2018.11.111.
48. Zhang, Y.; Zuo, T.; Cheng, Y.; Liaw, P.K. High-entropy Alloys with High Saturation Magnetization, Electrical Resistivity and Malleability. *Sci. Rep.* **2013**, *3*, 1455. https://doi.org/10.1038/srep01455.
49. Anantharaj, S.; Ede, S.R.; Sakthikumar, K.; Karthick, K.; Mishra, S.; Kundu, S. Recent Trends and Perspectives in Electrochemical Water Splitting with an Emphasis on Sulfide, Selenide, and Phosphide Catalysts of Fe, Co, and Ni: A Review. *ACS Catal.* **2016**, *6*, 8069–8097. https://doi.org/10.1021/acscatal.6b02479.
50. Liang, H.; Xu, M.; Asselin, E. Corrosion of monometallic iron- and nickel-based electrocatalysts for the alkaline oxygen evolution reaction: A review. *J. Power Sources* **2021**, *510*, 230387. https://doi.org/10.1016/j.jpowsour.2021.230387.
51. Gorlin, Y.; Jaramillo, T.F. A bifunctional nonprecious metal catalyst for oxygen reduction and water oxidation. *J. Am. Chem. Soc.* **2010**, *132*, 13612–13614.
52. Liu, Q.; Asiri, A.M.; Sun, X. Hematite nanorods array on carbon cloth as an efficient 3D oxygen evolution anode. *Electrochem. Commun.* **2014**, *49*, 21–24. https://doi.org/10.1016/j.elecom.2014.09.021.

53. Putra, R.P.; Horino, H.; Rzeznicka, I.I. An Efficient Electrocatalyst for Oxygen Evolution Reaction in Alkaline Solutions Derived from a Copper Chelate Polymer via In Situ Electrochemical Transformation. *Catalysts* **2020**, *10*, 233. https://doi.org/10.3390/catal10020233.
54. Medford, A.; Vojvodic, A.; Hummelshøj, J.S.; Voss, J.; Abild-Pedersen, F.; Studt, F.; Bligaard, T.; Nilsson, A.; Nørskov, J.K. From the Sabatier principle to a predictive theory of transition-metal heterogeneous catalysis. *J. Catal.* **2015**, *328*, 36–42. https://doi.org/10.1016/j.jcat.2014.12.033.